Methane's Solar Radiative Forcing

Rachael Emily Byrom[1] and Keith Peter Shine[2]

[1]CICERO Center for International Climate Research
[2]University of Reading

November 26, 2022

Abstract

Methane (CH_4) has significant absorption bands at wavelengths of 1.7, 2.3, 3.3 and 7.6 μm which absorb incoming solar 'shortwave' (SW) radiation and cause a radiative forcing (RF) of climate. This letter presents a comprehensive quantification of CH_4 SW RF using a narrow-band radiative transfer model to calculate spatially and monthly resolved estimates of the direct CH_4 SW effect and its impact on longwave (LW) RF via stratospheric temperature change. This significantly extends previous assessments. Calculations include satellite measurements of CH_4 distribution, spectrally-varying surface albedo and absorption of solar mid-infrared radiation by methane's 7.6 μm band. These factors substantially influence the SW effect; all-sky CH_4 SW tropopause instantaneous RF is significantly smaller than previous estimates at 0.002 W m^{-2} (±25%). In total, the CH_4 SW effect enhances CH_4 LW-only RF by 7% from 0.574 W m^{-2} to 0.613 W m^{-2} for a 750-1800 ppb perturbation.

Methane's Solar Radiative Forcing

R. E. Byrom[1*] and K. P. Shine[1]

[1]Department of Meteorology, University of Reading, UK

Corresponding author: Keith Shine (k.p.shine@reading.ac.uk)

*Current affiliation: CICERO Center for International Climate Research, Oslo, Norway

Key Points:

- The net effect of solar radiative forcing by CH_4 is assessed with spatially and temporally resolved calculations.
- CH_4 solar radiative forcing enhances CH_4 longwave-only radiative forcing by 7%.
- CH_4 solar radiative forcing is significantly sensitive to CH_4 profile specification, surface albedo and solar mid-infrared CH_4 absorption.

Abstract

Methane (CH_4) has significant absorption bands at wavelengths of 1.7, 2.3, 3.3 and 7.6 μm which absorb incoming solar 'shortwave' (SW) radiation and cause a radiative forcing (RF) of climate. This letter presents a comprehensive quantification of CH_4 SW RF using a narrow-band radiative transfer model to calculate spatially and monthly resolved estimates of the direct CH_4 SW effect and its impact on longwave (LW) RF via stratospheric temperature change. This significantly extends previous assessments. Calculations include satellite measurements of CH_4 distribution, spectrally-varying surface albedo and absorption of solar mid-infrared radiation by methane's 7.6 μm band. These factors substantially influence the SW effect; all-sky CH_4 SW tropopause instantaneous RF is significantly smaller than previous estimates at 0.002 W m^{-2} (±25%). In total, the CH_4 SW effect enhances CH_4 LW-only RF by 7% from 0.574 W m^{-2} to 0.613 W m^{-2} for a 750-1800 ppb perturbation.

Plain Language Summary

Radiative forcing is a widely used metric to quantitatively compare the strength of different drivers of climate change. It measures the perturbation to Earth's energy balance, such as that due to an increase in greenhouse gas concentrations. Most greenhouse gas forcings arise due to absorption of thermal infrared ("longwave") radiation, but greenhouse gases also absorb solar radiation. However, methane's solar radiative forcing has received relatively little attention. We present the most detailed calculation of methane's solar radiative forcing to date, when concentrations increase from pre-industrial to present day levels (750 – 1800 parts per billion). Our calculations are highly sensitive to the spatial and seasonal variation in surface albedo and methane's vertical profile, for which we exploit recent satellite measurements; we also quantify the effect of absorption of solar radiation at mid-infrared wavelengths. These factors significantly influence the magnitude of the forcing. Consequently, it is significantly smaller than previous estimates at 0.002 W m^{-2} (±25%). However, methane's absorption of solar radiation heats the stratosphere; this heating significantly modifies methane's longwave radiative forcing. When this effect is included we find that methane's absorption of solar radiation enhances methane's longwave radiative forcing by 7% from 0.574 W m^{-2} to 0.613 W m^{-2}.

1 Introduction

CH_4 is the second largest contributor to greenhouse gas RF (Forster et al., 2021). It predominantly interacts with thermal-infrared LW irradiances, but also absorbs incoming solar SW radiation, mainly at near-infrared (NIR) wavelengths (0.7 – 4μm). CH_4 SW absorption is not explicitly treated in radiative transfer codes in many climate models and its radiative effect has been relatively unexplored.

Recent studies have demonstrated the significance of CH_4 SW RF. Etminan et al., (2016) presented calculations using the Oslo line-by-line (LBL) code (OLBL; Myhre et al., 2006) for two atmospheric profiles (tropical/extratropical) to estimate global-mean tropopause CH_4 SW instantaneous RF (IRF) and its effect on LW stratospheric temperature-adjusted RF (SARF; see Myhre et al., 2013a for definitions). They demonstrated two key components of CH_4 SW RF. Firstly, CH_4 SW absorption bands exert a positive all-sky tropopause IRF of 0.03 W m^{-2} following a 750-1800 ppb perturbation. Secondly, the consequent stratospheric heating enhances the magnitude of CH_4 SARF. They reported that SW RF increases the Intergovernmental Panel on Climate Change (IPCC) Fifth Assessment Report (Myhre et al., 2013a) 1750-2011 CH_4 SARF by 15%. This revision underscored the importance of incorporating CH_4 SW absorption in RF calculations and emission metrics. They estimated a ±25% uncertainty due to a range of factors including: specification of surface albedo (α_s), computation of day-averaged forcings and their simple method of spatial and temporal averaging. Collins et al., (2018) later presented spatially-resolved calculations of CH_4 SW tropopause IRF using a narrow-band radiative transfer code and background climatologies from two Earth System Models (ESMs). For an 806-1760 ppb perturbation, they reported global annual-mean all-sky CH_4 SW tropopause IRFs of ≈0.026 W m^{-2} and demonstrated its distribution to depend significantly on NIR α_s. Collins et al., (2018) did not quantify the effect of SW absorption on SARF.

This letter presents the most detailed quantification of the CH_4 SW effect to date. A narrow-band radiative transfer model is used to calculate seasonally and spatially-resolved RF (Section 2). These calculations utilise satellite measurements of CH_4 and spectrally-resolved α_s to derive a best estimate of global annual-mean CH_4 SW IRF and SARF (Section 3). Comparisons with Etminan et al., (2016) and Collins et al., (2018) highlight key sensitivities, namely the effect of CH_4 SW

absorption at solar mid-infrared wavelengths, the vertical representation of CH_4 mole fraction and the specification of spectrally-resolved α_s.

2 Models, methods and data

RF calculations use the two-stream radiative transfer model, SOCRATES-RF (Checa-Garcia et al., 2018), which utilises the radiance core of the UK Met Office Suite Of Community RAdiative Transfer codes (SOCRATES, Edwards & Slingo, 1996; Manners et al., 2015) to compute IRF and SARF using the fixed dynamical heating (FDH) method (e.g. Ramaswamy et al., 2001).

SW IRFs are calculated using a 260-band spectral file (sp_sw_260_jm2) covering wavelengths from 0.17-10 μm. This file has been verified against LBL codes for a variety of scenarios by Walters et al., (2019) and is independently validated here against the LBL Reference Forward Model (RFM; Dudhia, 2017). It shows good agreement across a range of conditions. sp_sw_260_jm2 uses solar spectral data from the Naval Research Laboratory Solar Spectral Irradiance model (NRLSSI; Lean et al., 2005) averaged across 2000-2011. LW forcings use the standard broadband spectral file configuration (sp_lw_ga7) with 9 bands across 3.34-10000 μm (Walters et al., 2019). This lower resolution configuration was used due to the computational expense of performing spatially and seasonally resolved FDH calculations.

Gaseous absorption uses the correlated-k distribution method based on HITRAN2012 spectroscopic data (Rothman et al., 2013). SW and LW spectral gaseous overlap are treated using the equivalent extinction with correlated scaling method and the random overlap assumption, respectively. H_2O continuum absorption is based on MT_CKD 2.5 (Mlawer et al., 2012) with modifications in some NIR window regions using experimental data (Ptashnik et al., 2011, 2012). Calculations are conducted under clear-sky and all-sky conditions. Temperature, humidity and cloud fields are taken from ERA-interim reanalysis (Dee et al., 2011). Vertical cloud overlap is treated assuming random overlap; ice and water clouds are treated separately within three atmospheric layers. Aerosols are absent from calculations.

SOCRATES-RF adopts a tropopause pressure based on the parametric equation of Checa-Garcia et al., (2018) which describes a hemispherically-symmetric tropopause (see Equation S1). This prescribes annual-mean tropopause height following the climatological tropopause representation

by Hansen et al., (2005). A six-point Gaussian quadrature method is used to calculate the diurnal variation of solar radiation. All calculations are performed using monthly-mean input fields.

CH_4 mole fractions are derived from Michelson Interferometer for Passive Atmospheric Sounding (MIPAS) climatology (Hegglin et al., 2021), comprising zonal-mean values averaged between 2005-2012 from 300 hPa to 0.1 hPa at a 5° spatial resolution (see Text S2). This results in well-mixed tropospheric CH_4 and latitudinally-dependent, vertically-varying CH_4 at pressures below 300 hPa (Figure S3).

α_s is derived from 33 one-nm wavelength bands between 0.355-2.314 μm from the Scanning Imaging Absorption spectroMeter for Atmospheric CHartograhY (SCIAMACHY) Lambertian-equivalent reflectivity (LER) database (version 2.6; Tilstra et al., 2017) averaged between 2002-2012 at 0.5° x 0.5° spatial resolution. LER is defined as the reflectance of an isotropic surface required to match observed TOA reflectance in a clear-sky, aerosol-free Rayleigh scattering atmosphere (e.g., Kleipool et al., 2008). This dataset implicitly includes the effect of spatial and temporal variation in snow cover and sea-ice on spectral α_s (see Text S3). Given the lack of alternative observationally-based, spectrally-resolved global α_s datasets at $0.355 > \lambda > 2.314$ μm, this approach constructs a best estimate of spectral surface reflectance across 0.17-10 μm. LER data exhibit unrealistically low NIR α_s (≈0.001-0.008) over sea-surfaces, therefore these datapoints have been replaced with spectrally-varying α_s calculated using a SOCRATES internal subroutine (see Text S3). Consequently, α_s fields amalgamate SCIAMACHY and SOCRATES sea-surface α_s (henceforth referred to as SCIAMACHY-SSA) re-gridded to a 5° x 5° spatial resolution.

3.1 Clear-sky and all-sky CH_4 SW IRF

Table 1 shows global annual-mean SW IRF at top-of-atmosphere (TOA), tropopause and surface for a CH_4 perturbation from 750 to 1800 ppb, the approximate pre-industrial and present-day values used in Etminan et al., (2016). Corresponding LW and net IRFs are also shown to demonstrate the impact of SW absorption on total IRF.

	Clear-sky IRF (W m^{-2})			All-sky IRF (W m^{-2})		
	SW	**LW**	**Net**	**SW**	**LW**	**Net**
TOA	0.040	0.650	0.690	0.082	0.553	0.635
Tropopause	-0.038	0.674	0.636	0.002	0.578	0.580
Surface	-0.235	0.306	0.071	-0.163	0.180	0.017

Table 1: Global annual-mean clear-sky and all-sky SW, LW and net IRF at TOA, tropopause and surface following a 750-1800 ppb CH_4 perturbation. Derived using MIPAS CH_4 fields and SCIAMACHY-SSA α_s.

For clear-skies, SW IRF is positive at TOA (0.040 W m^{-2}) driven by enhanced absorption of surface-reflected radiation between the surface and TOA. At the tropopause and surface, SW IRF is negative due to a reduction in downward SW irradiance with enhanced CH_4 absorption in the stratosphere and troposphere. The surface SW IRF of -0.235 W m^{-2} counterbalances the surface LW IRF of 0.306 W m^{-2}, giving a net forcing of 0.071 W m^{-2}. Under all-sky conditions this offset is enhanced resulting in a net forcing of just 0.017 W m^{-2}. This demonstrates the importance of CH_4 SW absorption on surface energy budgets.

The all-sky TOA SW IRF increases from 0.040 W m^{-2} to 0.082 W m^{-2} due to absorption of increased reflected SW radiation. This mechanism is also responsible for the switch in sign of the tropopause SW IRF from -0.038 W m^{-2} to 0.002 W m^{-2}. This all-sky tropopause SW IRF is significantly smaller than Etminan et al., (2016) and Collins et al., (2018) (0.03 and ≈0.026 W m^{-2}, respectively). Section 3.2 addresses this disparity. Etminan et al., (2016) were the first to highlight the importance of cloud radiative effect (CRE) in determining the sign and magnitude of tropopause SW IRF; CRE increased their clear-sky SW tropopause IRF of -0.045 W m^{-2} by 0.075 W m^{-2} to a value of 0.03 W m^{-2}. The results presented here confirm the importance of CRE, albeit with a less pronounced increase (0.04 W m^{-2}).

Figure 1 shows the spatial distribution of annual-mean all-sky SW tropopause IRF (upper left) and the corresponding CRE (lower left). The distribution of SW IRF is comparable to Collins et al., (2018) exhibiting regions of maxima over the Arabian Peninsula and the Sahara (exceeding 0.20 W m^{-2}). Strong spatial gradients in the forcing are driven by spectrally-resolved NIR α_s for desert surfaces. As explained by Collins et al., (2018), such surfaces increase the reflection of

155 downwelling SW irradiance, enhancing the magnitude of tropospheric CH_4 SW absorption causing
156 a more positive IRF. CRE is predominantly positive with a localised maximum of 0.1 W m^{-2} off
157 the west coast of South America associated with oceanic stratocumulus cloud decks. Regions with
158 negative CRE dampen the influence of α_s on IRF magnitude, particularly across northern Africa
159 due to high NIR α_s of desert surfaces.
160
161 Notably, Collins et al., (2018) calculate positive (rather than negative) clear-sky tropopause SW
162 IRFs of 0.008 W m^{-2} and 0.011 W m^{-2} using their two ESM climatologies. They attribute positive
163 clear-sky forcings to the use of realistic surface conditions in their spatially-resolved simulations.
164 Consequently, CRE enhances their IRF by just 0.014 W m^{-2} and 0.018 W m^{-2}. Collins et al., (2018)
165 report a global-mean all-sky SW tropopause IRF of approximately 0.026 W m^{-2}, similar to the 0.03
166 W m^{-2} reported by Etminan et al., (2016). However, disagreement in the sign of clear-sky IRF and
167 the size of CRE indicate that this agreement is coincidental.
168
169
170

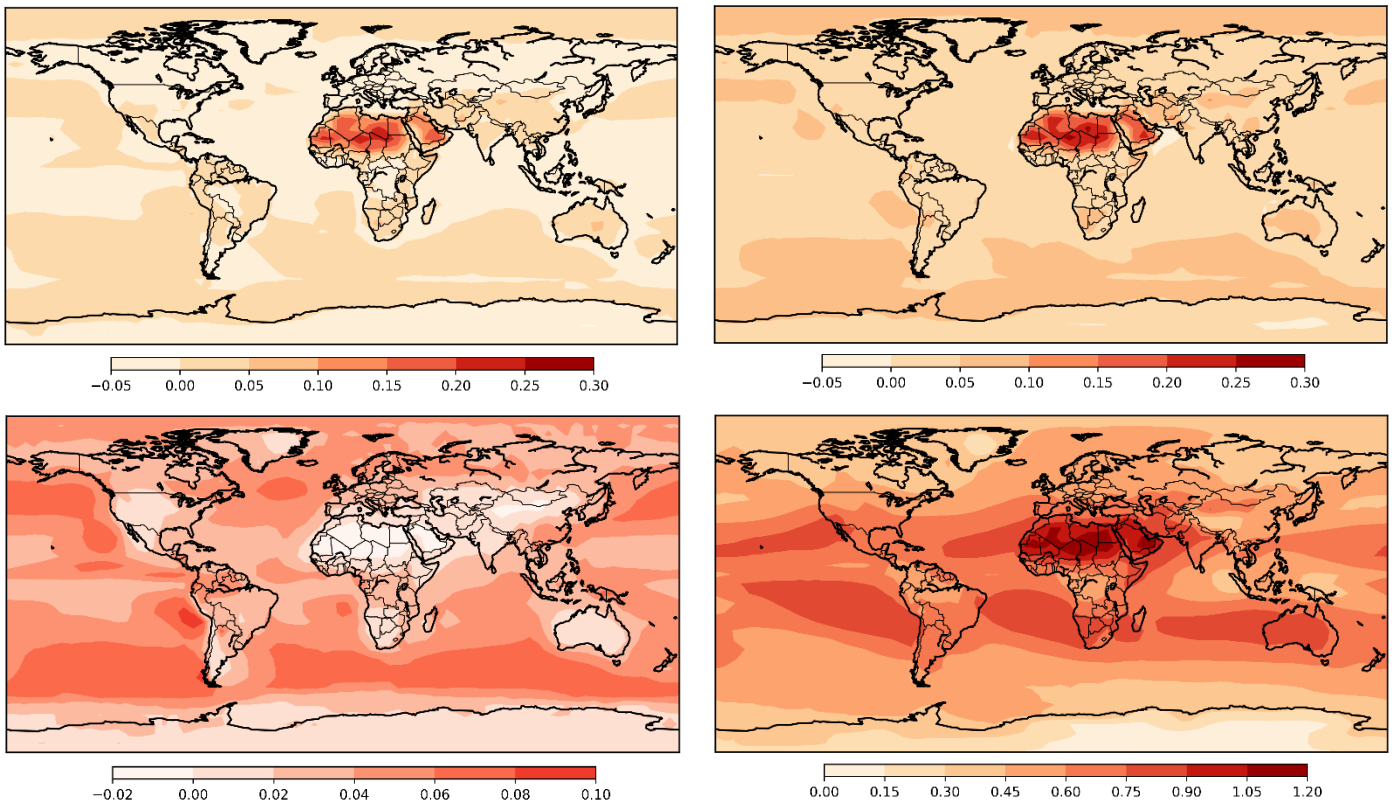

Figure 1: All annual-mean (W m^{-2}). Upper left: All-sky tropopause SW IRF. Lower left: Cloud radiative effect on tropopause SW IRF calculated as the difference between all-sky and clear-sky conditions. Upper right: Total all-sky SW RF at the tropopause derived as the difference between net SARF (i.e., LW SARF (including SW in FDH calculation) + SW IRF) and LW-only SARF. Lower right: All-sky net SARF at the tropopause. Derived using conditions stated in Table 1 caption. Global-mean forcings are given in Table 2.

171

172 **3.2 Explanation of reduction in size of all-sky CH_4 SW tropopause IRF**

173 The all-sky SW tropopause IRF of 0.002 W m^{-2} is significantly smaller than Etminan et al., (2016)
174 and Collins et al., (2018) due to a combination of factors that alter the relative importance of
175 downward and upward tropopause forcing components. As explained by Etminan et al., (2016)
176 (see also Shine et al., 2022), the tropopause SW IRF is a residual of reduced downward irradiance
177 (due to absorption in the stratosphere, which constitutes a negative IRF) and reduced upward
178 irradiance (due to absorption of surface-troposphere reflected irradiance in the troposphere, which

179 constitutes a positive IRF). The following sub-sections detail these factors using a range of
180 sensitivity tests.

181

182 **3.2.1 The representation of CH_4 vertical profiles**

183 CH_4 decreases with height above the tropopause due to chemical destruction. A realistic vertical
184 distribution in forcing calculations is necessary because stratospheric SW absorption contributes
185 significantly to the sign and magnitude of all-sky SW tropopause IRF (Figure S7).

186 Idealised sensitivity tests calculated using the RFM (not shown) and SOCRATES-RF demonstrate
187 the need for a realistic description of the spatial and temporal variability in stratospheric CH_4.
188 SOCRATES-RF tests were conducted using the Section 2 methodology, albeit with idealised
189 zonal-mean CH_4 mole fraction scale-heights from the CAM3.0 model (Collins et al., 2004), which
190 were used by Collins et al., (2018) (based on early 2-dimensional chemical model simulations –
191 see Text S4). These do not represent hemispherical and seasonal differences in stratospheric CH_4.

192 Using 'CAM3.0' scale-heights results in an all-sky SW tropopause IRF of 0.009 W m^{-2}. The
193 equivalent calculation using MIPAS mole fractions gives an IRF of 0.002 W m^{-2} (Table 1). This
194 difference originates from the size of the downward SW forcing component. With 'MIPAS', more
195 CH_4 is present in the stratosphere compared to CAM3.0. MIPAS CH_4 mole fractions vary monthly
196 and exhibit a variable rate of decrease with height at each latitude (see Figure S6) unlike CAM3.0's
197 smooth exponential decrease (see Figure S5). MIPAS values are at least 2.5 times larger than
198 CAM3.0 values at 300 hPa at 0°. This disparity increases poleward to over 10 times larger at 300
199 hPa at 60° and 90° N/S. MIPAS values increase stratospheric CH_4 SW absorption at both pre-
200 industrial and present-day levels, causing a more negative downward IRF at the tropopause.
201 Hence, the positive upward forcing component (due to CRE) makes the MIPAS forcing only
202 weakly positive, but decisively positive for CAM3.0.

203

204 **3.2.2 Impact of CH_4 absorption between 5-10 µm**

205 Solar spectral irradiance extends beyond the NIR; around 5.4 W m^{-2} occurs in the 5–10 µm region.
206 Although only about 0.5% of total solar irradiance, this spectral region contains the strong 7.6 µm
207 CH_4 absorption band (primarily responsible for CH_4 LW RF). In exploratory calculations using

CAM3.0 CH_4 profiles and spectrally-constant α_s fields from ERA-interim reanalysis data (Dee et al., 2011), the 5-10 μm all-sky CH_4 SW tropopause IRF is found to be -0.004 W m^{-2} compared to the 0.17-10 μm value of 0.016 W m^{-2}. The negative forcing demonstrates that this spectral region mainly impacts stratospheric absorption. Neglecting this contribution would overestimate the all-sky SW tropopause IRF by 25%, for this configuration; hence the 5-10 μm region is included in calculations presented here. Both Etminan et al., (2016) and Collins et al., (2018) use an upper wavelength limit of 5 μm. The spectral nature of CH_4 SW IRF was considered in detail in Etminan et al., (2016); Figure S7 extends this to include methane's 7.6 μm band.

3.2.3 Sensitivity to spectrally-varying albedo

The spatial and spectral variation in α_s depends on factors including surface type, season and solar zenith angle. Tests conducted using the Reading LBL model RFMDISORT (see Table 7 of Collins et al., 2006) and SOCRATES-RF demonstrate the importance of spectrally-varying α_s in controlling the amount of surface-reflected SW radiation absorbed by CH_4. The use of spectrally-constant ERA-interim α_s in forcing calculations overestimates the reflected SW radiation absorbed by CH_4 predominantly in the polar regions, yielding a global-mean all-sky SW tropopause IRF of 0.016 W m^{-2} compared to 0.009 W m^{-2} using SCIAMACHY-SSA α_s (both calculated using SOCRATES-RF with CAM3.0 CH_4; see Figure S8).

Both Etminan et al., (2016) and Collins et al., (2018) incorporate spectrally-varying α_s. Etminan et al., (2016) use broadband values taken from OsloCTM2 simulations (Myhre et al., 2013b). Collins et al., (2018) use land and snow α_s "obtained from climate model grid spectral seven-band Moderate Resolution Imaging Spectroradiometer bi-directional reflectance distribution functions" covering the 0.620-2.155 μm wavelength range. Here, the use of SCIAMACHY α_s data (with 33 bands across 0.355-2.314 μm) provides a better resolved description of land and sea-ice α_s. The representation of ocean α_s here (Section 2) and in Collins et al., (2018) is of similar complexity, based on Cox and Munk (1954).

Summarising, the combined effect of the above sensitivities results in a significantly smaller all-sky CH_4 SW tropopause IRF compared to earlier estimates. MIPAS fields significantly improve the representation of the spatial and temporal variation in stratospheric CH_4, SCIAMACHY-SSA

provides a more highly spectrally-resolved description of α_s and SOCRATES includes solar CH_4 absorption between 5-10 μm.

3.3 Impact of stratospheric CH_4 SW absorption on SARF

The total SW effect is quantified by comparing the net SARF, calculated due to both SW and LW absorption, against the SARF calculated due to LW absorption alone. Table 2 shows all-sky SW IRF, LW SARF (where SW absorption is *included* in the FDH calculation), net SARF (SW IRF plus LW SARF) and LW-only SARF (where SW absorption is *excluded* from the FDH calculation). The SW forcing is only minimally affected by the temperature change; hence SW IRF and SW SARF are identical.

	All-sky CH_4 RF (W m^{-2})			
	SW IRF	**LW SARF**	**Net SARF**	**LW-only SARF**
TOA	0.082	0.530	0.613	0.574
Tropopause	0.002	0.611	0.613	0.574
Surface	-0.163	0.181	0.018	0.179

Table 2: Global annual-mean all-sky TOA, tropopause and surface SW IRF, LW SARF (including SW heating rates in the FDH calculation), net SARF (SW IRF + LW SARF) and LW-only SARF (excluding SW heating rates in the FDH calculation). Derived using conditions stated in Table 1 caption.

The tropopause SW IRF of 0.002 W m^{-2} is only a small fraction (0.3%) of net SARF (0.613 W m^{-2}). However, when SW absorption is included in the calculation of stratospheric temperature adjustment, net SARF increases by 7% to 0.613 W m^{-2} from the LW-only SARF of 0.574 W m^{-2}. This difference (0.04 W m^{-2}) is 20 times larger than the tropopause SW IRF itself, emphasising that the contribution of SW absorption to net SARF should not be assessed by considering the impact on SW fluxes alone.

Figure 2 compares the stratospheric temperature difference (ΔT) calculated using FDH for LW-only and LW plus SW heating rates. In the LW-only case (upper panel), increased CH_4 leads to a cooling across most of the stratosphere, exceeding 0.2 K in the upper stratosphere. A small

warming is evident above the tropical tropopause; however, this does not counterbalance the impact of the cooling on downward LW irradiance at the tropopause, which is found to slightly decrease the LW forcing from 0.578 W m^{-2} (Table 1) to 0.574 W m^{-2} (Table 2). When SW absorption is included (lower panel), the cooling is reduced across the entire stratosphere and reverses sign over much of the lower stratosphere, giving a strong warming reaching a maximum ΔT of 0.5 K above the tropical tropopause. As a result, the LW IRF of 0.578 W m^{-2} (Table 1) is increased to a SARF value of 0.611 W m^{-2} (Table 2). This increases further to 0.613 W m^{-2} when the SW IRF is included.

The temperature change is consistent with the idealised experiments of Modak et al., (2018) in which SW absorption causes stratospheric warming of around 0.8 K, peaking at 100 hPa for a 10x increase in CH_4. The peak 0.5 K warming calculated here is equivalent to a warming of around 0.05 $decade^{-1}$, if it occurred at a steady rate.

Figure 1 (upper right) presents the first spatially-resolved calculation of the total CH_4 SW radiative effect (to our knowledge) including both direct all-sky tropopause SW IRF and the effect of SW absorption on stratospheric temperatures. The inclusion of SW absorption increases net SARF (Figure 1, lower right) largely across the entire globe. Figure 1 (upper right) shows the enhancement is largest across northern Africa and the Arabian Peninsula, but also in regions with extensive low cloud, such as the southern oceans.

The total SW effect of 7% is smaller than the 15% reported by Etminan et al., (2016). The difference is largely explained by the substantial difference in the magnitude of the SW tropopause IRF (0.002 W m^{-2} compared to 0.03 W m^{-2}), but also by the magnitude of stratospheric temperature-adjustment. Etminan et al., (2016) find this process has a slightly more negative effect on their estimate of CH_4 LW IRF, decreasing it by 2% from 0.516 W m^{-2} to 0.504 W m^{-2}. Considering the total SW effect is measured relative to adjusted LW-only SARF, this yields a larger percentage increase from their LW-only SARF (0.504 W m^{-2}) to their net SARF (0.582 W m^{-2}). In addition to the sensitivities addressed in Section 3.2, the total CH_4 SW effect also depends on state variables (and their spatial and temporal variation) that affect CH_4 LW forcing and FDH adjustment, including temperature, humidity and clouds. Text S5 discusses uncertainty associated with the calculation of SW tropopause IRF and LW SARF. Using the root-sum-square method, a total uncertainty of ±12% is attributed to LW SARF and a total uncertainty of ±25% is tentatively

attributed to SW tropopause IRF (see Table S2). Given the highly sensitive nature of CH_4 SW tropopause IRF, we believe that Etminan et al.,'s ±25% estimate of uncertainty was too low, hence despite the improved methodology here, we adopt the same overall uncertainty. In total, given that the CH_4 SW effect is about 6% of the net SARF, this yields a total uncertainty of around ±13% in net CH_4 SARF.

An alternative perspective on CH_4 SW RF can be gained by examining TOA forcings which is more analogous to effective radiative forcing (ERF) estimates derived from ESMs (Shine et al., 2022). For SARF, the net TOA and tropopause forcings are identical (Table 2) as is the total impact of the SW forcing (i.e., 7%). However, unlike the tropopause IRF, the SW TOA IRF is not a residual of changes in upward and downward irradiance and a more confident assessment is possible. TOA SW IRF is 0.082 W m^{-2} (or 13% of TOA net SARF). Stratospheric heating by SW absorption leads to an increase in TOA LW irradiance which drives a reduction in TOA LW SARF from 0.574 to 0.530 W m^{-2} (Table 2).

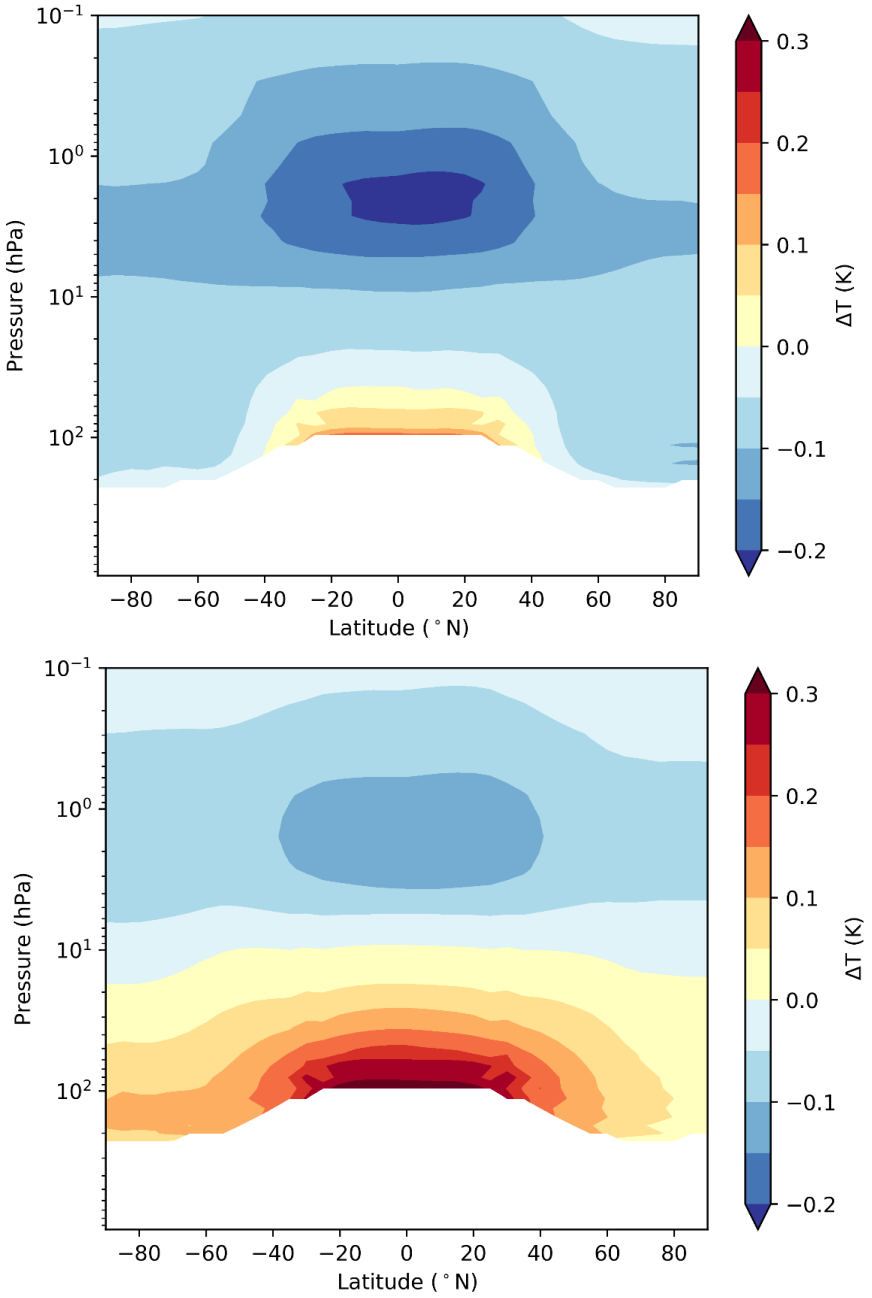

Figure 2: Annual zonal-mean ΔT (in K) following stratospheric temperature adjustment calculated using FDH for LW-only (upper panel) and LW plus SW heating rates (lower panel). Small oscillations in ΔT occur near the tropopause when SW heating rates are found in stratospheric temperature adjustment, therefore data in the lower plot have been smoothed. Derived using conditions stated in Table 1 caption.

303

304 4. Discussion

305 Accurate quantification of CH_4 SW RF is dependent on spatially-resolved specifications of CH_4
306 vertical profiles, CRE and spectrally-resolved α_s to capture their collective heterogeneous effect
307 on SW absorption. It is also dependent on inclusion of solar mid-infrared absorption. Further
308 studies that incorporate these factors are needed, particularly to constrain the sign and magnitude
309 of clear-sky tropopause IRF.

310 A multi-model intercomparison would help quantify the accuracy of CH_4 SW absorption in ESM
311 radiation schemes; Text S5 presents evidence that CH_4 SW IRF is significantly underestimated in
312 some such schemes. As emphasised here, the accuracy of CH_4 SW ERF also depends on the way
313 ESMs represent CH_4 vertical distribution and spectrally-varying α_s. This is particularly important
314 with respect to the calculation of individual adjustments. Adjustments for a tripling of CH_4 have
315 been calculated by Smith et al., (2018) in 11 ESMs using radiative kernels and the RFMIP (Pincus
316 et al., 2016) fixed-SST approach. Four of these ESMs included CH_4 SW absorption bands.
317 Although this is a small sample of models, the inclusion or omission of these bands appears to
318 dictate the magnitude of H_2O adjustment and whether stratospheric temperature and cloud
319 adjustments have a negative or positive effect on CH_4 forcing; this could only be confidently
320 established if those models were run without these bands. Models that include CH_4 SW absorption
321 simulate a negative stratospheric temperature adjustment to a CH_4 perturbation, consistent with
322 the sign derived here from a TOA perspective. Although uncertainties are large in Smith et al.,
323 (2018), there is an indication that the total CH_4 adjustment is negative when SW absorption is
324 included and positive when it is not.

325 IPCC AR6 (Forster et al., 2021) calculate CH_4 SARF using the simplified expression of
326 Meinshausen et al., (2020) which incorporates the total CH_4 SW effect of 15% estimated by
327 Etminan et al., (2016). The CH_4 ERF is estimated using the tropospheric adjustments of Smith et
328 al., (2018) from the 4 ESMs that include CH_4 SW absorption. Overall, these adjustments reduce
329 the ERF relative to TOA IRF by -14% (± 15%; Forster et al., 2021). According to the total CH_4
330 SW effect of 7% presented here, IPCC AR6 CH_4 SARF and CH_4 ERF are both slightly
331 overestimated. However, as stated above, the magnitude of tropospheric CH_4 adjustments are

uncertain; further assessment is needed by ESMs that include validated treatment of CH_4 SW absorption.

5. Conclusions

Accurate quantification of CH_4 SW RF depends on realistic spatial and temporal representations of CH_4 vertical profiles, CRE, spectrally-resolved α_s and inclusion of solar mid-infrared CH_4 absorption. At the surface, CH_4 SW IRF counteracts around 90% of CH_4 LW IRF resulting in a residual net IRF of 0.017 W m^{-2}. At the tropopause, CH_4 SW IRF is highly sensitive to the magnitude of the upward and downward forcing components and is significantly smaller than previous estimates at 0.002 W m^{-2} (±25%). However, the total CH_4 SW effect can only be fully quantified when the impact of stratospheric CH_4 SW absorption is included in the calculation of CH_4 SARF. Consequently, inclusion of SW absorption enhances the LW-only SARF by 7%, from 0.574 W m^{-2} to 0.613 W m^{-2} for a 750 to 1800 ppb perturbation. An alternative TOA perspective demonstrates that the SW IRF is 13% of TOA net SARF; the total effect of SW absorption is still 7% (i.e., in agreement with the tropopause view) as a result of stratospheric temperature adjustment. This indicates that the perception of the role of SW RF (particularly the direct impact of SW IRF and the impact of stratospheric temperature adjustment) depends on the perspective taken. In the ERF framework, the TOA view is becoming more prevalent.

Acknowledgments

REB would like to thank the NERC Scenario Doctoral Training Partnership for funding her PhD studentship. We thank William D. Collins (University of California, Berkeley) for several valuable discussions in the early stages of this work. We also thank William Collins (University of Reading), Michaela Hegglin and Amanda Maycock for their input and Ramiro Checa-Garcia, Jonathan Elsey and James Manners for their help in model development. ERA-interim renalysis, SCIAMACHY LER and MIPAS CH_4 climatology data are available through Dee et al., (2011), Tilstra et al., (2017) and Hegglin et al., (2021), respectively.

References

Checa-Garcia, R., Hegglin, M. I., Kinnison, D., Plummer, D. A., & Shine, K. P. (2018). Historical Tropospheric and Stratospheric Ozone Radiative Forcing Using the CMIP6 Database. *Geophysical Research Letters*, *45*(7), 3264-3273. https://doi.org/https://doi.org/10.1002/2017GL076770

Collins, W., Rasch, P. J., Boville, B. A., McCaa, J., Williamson, D. L., Kiehl, J. T., Briegleb, B. P., Bitz, C., Lin, S.-J., Zhang, M., and Dai, Y. . (2004). *Description of the NCAR Community Atmosphere Model (CAM 3.0) (No. NCAR/TN-464+STR)*.

Collins, W. D., Ramaswamy, V., Schwarzkopf, M. D., Sun, Y., Portmann, R. W., Fu, Q., et al. (2006). Radiative forcing by well-mixed greenhouse gases: Estimates from climate models in the Intergovernmental Panel on Climate Change (IPCC) Fourth Assessment Report (AR4). *Journal of Geophysical Research: Atmospheres*, *111*(D14). https://doi.org/https://doi.org/10.1029/2005JD006713

Collins, W. D., Feldman, D. R., Kuo, C., & Nguyen, N. H. (2018). Large regional shortwave forcing by anthropogenic methane informed by Jovian observations. *Science Advances*, *4*(9), eaas9593. https://doi.org/doi:10.1126/sciadv.aas9593

Cox, C., & Munk, W. (1954). Measurement of the Roughness of the Sea Surface from Photographs of the Sun's Glitter. *Journal of the Optical Society of America*, *44*(11), 838-850. https://doi.org/10.1364/JOSA.44.000838

Dee, D. P., Uppala, S. M., Simmons, A. J., Berrisford, P., Poli, P., Kobayashi, S., et al. (2011). The ERA-Interim reanalysis: configuration and performance of the data assimilation system. *Quarterly Journal of the Royal Meteorological Society*, *137*(656), 553-597. https://doi.org/https://doi.org/10.1002/qj.828

Dudhia, A. (2017). The Reference Forward Model (RFM). *Journal of Quantitative Spectroscopy and Radiative Transfer*, *186*, 243-253. https://doi.org/https://doi.org/10.1016/j.jqsrt.2016.06.018

Edwards, J. M., & Slingo, A. (1996). Studies with a flexible new radiation code. I: Choosing a configuration for a large-scale model. *Quarterly Journal of the Royal Meteorological Society*, *122*(531), 689-719. https://doi.org/https://doi.org/10.1002/qj.49712253107

Etminan, M., Myhre, G., Highwood, E. J., & Shine, K. P. (2016). Radiative forcing of carbon dioxide, methane, and nitrous oxide: A significant revision of the methane radiative forcing. *Geophysical Research Letters*, *43*(24), 12,614-612,623. https://doi.org/https://doi.org/10.1002/2016GL071930

Forster, P., T. Storelvmo, K. Armour, W. Collins, J.-L. Dufresne, D. Frame, D.J. Lunt, T. Mauritsen, M.D. Palmer, M. Watanabe, M. Wild, and H. Zhang. (2021). *The Earth's Energy Budget, Climate Feedbacks, and Climate Sensitivity. In Climate Change 2021: The Physical Science Basis. Contribution of Working Group I to the Sixth Assessment Report of the Intergovernmental Panel on Climate Change*.

Hansen, J., Sato, M., Ruedy, R., Nazarenko, L., Lacis, A., Schmidt, G. A., et al. (2005). Efficacy of climate forcings. *Journal of Geophysical Research: Atmospheres*, *110*(D18). https://doi.org/https://doi.org/10.1029/2005JD005776

Hegglin, M. I., Tegtmeier, S., Anderson, J., Bourassa, A. E., Brohede, S., Degenstein, D., et al. (2021). Overview and update of the SPARC Data Initiative: comparison of stratospheric composition measurements from satellite limb sounders. *Earth Syst. Sci. Data*, *13*(5), 1855-1903. https://doi.org/10.5194/essd-13-1855-2021

Kleipool, Q. L., Dobber, M. R., de Haan, J. F., & Levelt, P. F. (2008). Earth surface reflectance climatology from 3 years of OMI data. *Journal of Geophysical Research: Atmospheres*, *113*(D18). https://doi.org/https://doi.org/10.1029/2008JD010290

Lean, J., Rottman, G., Harder, J., & Kopp, G. (2005). SORCE Contributions to New Understanding of Global Change and Solar Variability. *Solar Physics*, *230*(1), 27-53. https://doi.org/10.1007/s11207-005-1527-2

Manners, J., Edwards, J. M., Hill, P., and Thelen, J.-C. (2015). *SOCRATES Technical Guide Suite Of Community RAdiative Transfer codes based on Edwards and Slingo*.

Meinshausen, M., Nicholls, Z. R. J., Lewis, J., Gidden, M. J., Vogel, E., Freund, M., et al. (2020). The shared socio-economic pathway (SSP) greenhouse gas concentrations and

their extensions to 2500. *Geosci. Model Dev.*, *13*(8), 3571-3605. https://doi.org/10.5194/gmd-13-3571-2020

Mlawer, E. J., Payne, V. H., Moncet, J.-L., Delamere, J. S., Alvarado, M. J., & Tobin, D. C. (2012). Development and recent evaluation of the MT_CKD model of continuum absorption. *Philosophical Transactions of the Royal Society A: Mathematical, Physical and Engineering Sciences*, *370*(1968), 2520-2556. https://doi.org/doi:10.1098/rsta.2011.0295

Modak, A., Bala, G., Caldeira, K., & Cao, L. (2018). Does shortwave absorption by methane influence its effectiveness? *Climate Dynamics*, *51*(9), 3653-3672. https://doi.org/10.1007/s00382-018-4102-x

Myhre, G., Stordal, F., Gausemel, I., Nielsen, C. J., & Mahieu, E. (2006). Line-by-line calculations of thermal infrared radiation representative for global condition: CFC-12 as an example. *Journal of Quantitative Spectroscopy and Radiative Transfer*, *97*(3), 317-331. https://doi.org/10.1016/j.jqsrt.2005.04.015

Myhre, G., Shindell, D., Bréon, F.-M., Collins, W., Fuglestvedt, J., Huang, J., Koch, D., Lamarque, J.-F., Lee, D., Mendoza, B., Nakajima, T., Robock, A., Stephens, G., Takemura, T., and Zhang, H. . (2013a). *Anthropogenic and Natural Radiative Forcing. In: Climate Change 2013: The Physical Science Basis. Contribution of Working Group I to the Fifth Assessment Report of the Intergovernmental Panel on Climate Change* C. U. Press.

Myhre, G., Samset, B. H., Schulz, M., Balkanski, Y., Bauer, S., Berntsen, T. K., et al. (2013b). Radiative forcing of the direct aerosol effect from AeroCom Phase II simulations. *Atmos. Chem. Phys.*, *13*(4), 1853-1877. https://doi.org/10.5194/acp-13-1853-2013

Pincus, R., Forster, P. M., & Stevens, B. (2016). The Radiative Forcing Model Intercomparison Project (RFMIP): experimental protocol for CMIP6. *Geosci. Model Dev.*, *9*(9), 3447-3460. https://doi.org/10.5194/gmd-9-3447-2016

Ptashnik, I. V., McPheat, R. A., Shine, K. P., Smith, K. M., & Williams, R. G. (2011). Water vapor self-continuum absorption in near-infrared windows derived from laboratory

measurements. *Journal of Geophysical Research: Atmospheres*, *116*(D16). https://doi.org/https://doi.org/10.1029/2011JD015603

Ptashnik, I. V., McPheat, R. A., Shine, K. P., Smith, K. M., & Williams, R. G. (2012). Water vapour foreign-continuum absorption in near-infrared windows from laboratory measurements. *Philosophical Transactions of the Royal Society A: Mathematical, Physical and Engineering Sciences*, *370*(1968), 2557-2577. https://doi.org/doi:10.1098/rsta.2011.0218

Ramaswamy, V., Boucher, O., Haigh, J., Hauglustaine, D., Haywood, J., and Myhre, G. et al., . (2001). *Radiative Forcing of Climate Change. In: Climate Change 2001: The Scientific Basis. Contirbution of Working Group I to the Third Assessment Report of the Intrgovernmental Panel on Climate Change*.

Rothman, L. S., Gordon, I. E., Babikov, Y., Barbe, A., Chris Benner, D., Bernath, P. F., et al. (2013). The HITRAN2012 molecular spectroscopic database. *Journal of Quantitative Spectroscopy and Radiative Transfer*, *130*, 4-50. https://doi.org/10.1016/j.jqsrt.2013.07.002

Shine, K. P., Byrom, R. E., and Checa-Garcia, R. (2022). Conceptual understanding of shortwave radiative forcing by greenhouse gases. *Atmospheric Science Letters (submitted)*.

Smith, C. J., Kramer, R. J., Myhre, G., Forster, P. M., Soden, B. J., Andrews, T., et al. (2018). Understanding Rapid Adjustments to Diverse Forcing Agents. *Geophysical Research Letters*, *45*(21), 12,023-012,031. https://doi.org/10.1029/2018GL079826

Tilstra, L. G., Tuinder, O. N. E., Wang, P., & Stammes, P. (2017). Surface reflectivity climatologies from UV to NIR determined from Earth observations by GOME-2 and SCIAMACHY. *Journal of Geophysical Research: Atmospheres*, *122*(7), 4084-4111. https://doi.org/10.1002/2016JD025940

Walters, D., Baran, A. J., Boutle, I., Brooks, M., Earnshaw, P., Edwards, J., et al. (2019). The Met Office Unified Model Global Atmosphere 7.0/7.1 and JULES Global Land 7.0 configurations. *Geosci. Model Dev.*, *12*(5), 1909-1963. https://doi.org/10.5194/gmd-12-1909-2019

References From the Supporting Information

Anisman, L. O., Chubb, K. L., Elsey, J., Al-Refaie, A., Changeat, Q., Yurchenko, S. N., et al. (2022). Cross-sections for heavy atmospheres: H2O continuum. *Journal of Quantitative Spectroscopy and Radiative Transfer*, *278*, 108013. https://doi.org/https://doi.org/10.1016/j.jqsrt.2021.108013

Briegleb, B., & Ramanathan, V. (1982). Spectral and Diurnal Variations in Clear Sky Planetary Albedo. *Journal of Applied Meteorology (1962-1982)*, *21*(8), 1160-1171. http://www.jstor.org/stable/26180502

Checa-Garcia, R., Hegglin, M. I., Kinnison, D., Plummer, D. A., & Shine, K. P. (2018). Historical Tropospheric and Stratospheric Ozone Radiative Forcing Using the CMIP6 Database. *Geophysical Research Letters*, *45*(7), 3264-3273. https://doi.org/https://doi.org/10.1002/2017GL076770

Choi, W. K., & Holton, J. R. (1991). Transport of N_2O in the stratosphere related to the equatorial semiannual oscillation. *Journal of Geophysical Research: Atmospheres*, *96*(D12), 22543-22557. https://doi.org/https://doi.org/10.1029/91JD02263

Collins, W., Rasch, P. J., Boville, B. A., McCaa, J., Williamson, D. L., Kiehl, J. T., Briegleb, B. P., Bitz, C., Lin, S.-J., Zhang, M., and Dai, Y. . (2004). *Description of the NCAR Community Atmosphere Model (CAM 3.0) (No. NCAR/TN-464+STR)*.

Collins, W. D., Feldman, D. R., Kuo, C., & Nguyen, N. H. (2018). Large regional shortwave forcing by anthropogenic methane informed by Jovian observations. *Science Advances*, *4*(9), eaas9593. https://doi.org/doi:10.1126/sciadv.aas9593

Dee, D. P., Uppala, S. M., Simmons, A. J., Berrisford, P., Poli, P., Kobayashi, S., et al. (2011). The ERA-Interim reanalysis: configuration and performance of the data assimilation system. *Quarterly Journal of the Royal Meteorological Society*, *137*(656), 553-597. https://doi.org/https://doi.org/10.1002/qj.828

Errera, Q., Ceccherini, S., Christophe, Y., Chabrillat, S., Hegglin, M. I., Lambert, A., et al. (2016). Harmonisation and diagnostics of MIPAS ESA CH_4 and N_2O profiles using data assimilation. *Atmos. Meas. Tech.*, *9*(12), 5895-5909. https://doi.org/10.5194/amt-9-5895-2016

503 Etminan, M., Myhre, G., Highwood, E. J., & Shine, K. P. (2016). Radiative forcing of carbon
504 dioxide, methane, and nitrous oxide: A significant revision of the methane radiative
505 forcing. *Geophysical Research Letters*, *43*(24), 12,614-612,623.
506 https://doi.org/https://doi.org/10.1002/2016GL071930

507 Freckleton, R. S., Highwood, E. J., Shine, K. P., Wild, O., Law, K. S., & Sanderson, M. G.
508 (1998). Greenhouse gas radiative forcing: Effects of averaging and inhomogeneities in
509 trace gas distribution. *Quarterly Journal of the Royal Meteorological Society*, *124*(550),
510 2099-2127. https://doi.org/https://doi.org/10.1002/qj.49712455014

511 Hale, G. M., & Querry, M. R. (1973). Optical Constants of Water in the 200-nm to 200-µm
512 Wavelength Region. *Applied Optics*, *12*(3), 555-563.
513 https://doi.org/10.1364/AO.12.000555

514 Hansen, J., Sato, M., Ruedy, R., Nazarenko, L., Lacis, A., Schmidt, G. A., et al. (2005). Efficacy
515 of climate forcings. *Journal of Geophysical Research: Atmospheres*, *110*(D18).
516 https://doi.org/https://doi.org/10.1029/2005JD005776

517 Hegglin, M. I., Tegtmeier, S., Anderson, J., Bourassa, A. E., Brohede, S., Degenstein, D., et al.
518 (2021). Overview and update of the SPARC Data Initiative: comparison of stratospheric
519 composition measurements from satellite limb sounders. *Earth Syst. Sci. Data*, *13*(5),
520 1855-1903. https://doi.org/10.5194/essd-13-1855-2021

521 Hodnebrog, Ø., Etminan, M., Fuglestvedt, J. S., Marston, G., Myhre, G., Nielsen, C. J., et al.
522 (2013). Global warming potentials and radiative efficiencies of halocarbons and related
523 compounds: A comprehensive review. *Reviews of Geophysics*, *51*(2), 300-378.
524 https://doi.org/https://doi.org/10.1002/rog.20013

525 Hodnebrog, Ø., Myhre, G., Kramer, R. J., Shine, K. P., Andrews, T., Faluvegi, G., et al. (2020).
526 The effect of rapid adjustments to halocarbons and N_2O on radiative forcing. *npj Climate*
527 *and Atmospheric Science*, *3*(1), 43. https://doi.org/10.1038/s41612-020-00150-x

528 Hogan, R. J., & Matricardi, M. (2020). Evaluating and improving the treatment of gases in
529 radiation schemes: the Correlated K-Distribution Model Intercomparison Project
530 (CKDMIP). *Geosci. Model Dev.*, *13*(12), 6501-6521. https://doi.org/10.5194/gmd-13-
531 6501-2020

Huang, X., Chen, X., Flanner, M., Yang, P., Feldman, D., & Kuo, C. (2018). Improved Representation of Surface Spectral Emissivity in a Global Climate Model and Its Impact on Simulated Climate. *Journal of Climate*, *31*(9), 3711-3727. https://doi.org/10.1175/jcli-d-17-0125.1

IFS Documentation CY47R1. (2020). Part IV: Physical Processes. In *IFS Documentation CY47R1*. ECMWF. https://www.ecmwf.int/node/19748

Jerlov, N. G. (1976). *Marine Optics* (2 ed.). Elsevier Scientific Pub. Co., Amsterdam, New York. ISBN: 9780080870502

Laeng, A., Plieninger, J., von Clarmann, T., Grabowski, U., Stiller, G., Eckert, E., et al. (2015). Validation of MIPAS IMK/IAA methane profiles. *Atmos. Meas. Tech.*, *8*(12), 5251-5261. https://doi.org/10.5194/amt-8-5251-2015

Oreopoulos, L., Mlawer, E., Delamere, J., Shippert, T., Cole, J., Fomin, B., et al. (2012). The Continual Intercomparison of Radiation Codes: Results from Phase I. *Journal of Geophysical Research: Atmospheres*, *117*(D6). https://doi.org/https://doi.org/10.1029/2011JD016821

Pincus, R., Mlawer, E. J., Oreopoulos, L., Ackerman, A. S., Baek, S., Brath, M., et al. (2015). Radiative flux and forcing parameterization error in aerosol-free clear skies. *Geophysical Research Letters*, *42*(13), 5485-5492. https://doi.org/https://doi.org/10.1002/2015GL064291

Plieninger, J., Laeng, A., Lossow, S., von Clarmann, T., Stiller, G. P., Kellmann, S., et al. (2016). Validation of revised methane and nitrous oxide profiles from MIPAS–ENVISAT. *Atmos. Meas. Tech.*, *9*(2), 765-779. https://doi.org/10.5194/amt-9-765-2016

Ricaud, P., Sič, B., El Amraoui, L., Attié, J. L., Zbinden, R., Huszar, P., et al. (2014). Impact of the Asian monsoon anticyclone on the variability of mid-to-upper tropospheric methane above the Mediterranean Basin. *Atmos. Chem. Phys.*, *14*(20), 11427-11446. https://doi.org/10.5194/acp-14-11427-2014

Roesch, A., Wild, M., Pinker, R., & Ohmura, A. (2002). Comparison of spectral surface albedos and their impact on the general circulation model simulated surface climate. *Journal of*

Geophysical Research: Atmospheres, *107*(D14), ACL 13-11-ACL 13-18. https://doi.org/https://doi.org/10.1029/2001JD000809

Séférian, R., Baek, S., Boucher, O., Dufresne, J. L., Decharme, B., Saint-Martin, D., & Roehrig, R. (2018). An interactive ocean surface albedo scheme (OSAv1.0): formulation and evaluation in ARPEGE-Climat (V6.1) and LMDZ (V5A). *Geosci. Model Dev.*, *11*(1), 321-338. https://doi.org/10.5194/gmd-11-321-2018

SPARC. (2017). *The SPARC Data Initiative: Assessment of stratospheric trace gas and aerosol climatologies from satellite limb sounders* (SPARC Report No. 8, WCRP-5/2017, Issue. www.sparc-climate.org/publications/sparc reports/sparc-report-no-8/

Tilstra, L. G., Tuinder, O. N. E., Wang, P., & Stammes, P. (2017). Surface reflectivity climatologies from UV to NIR determined from Earth observations by GOME-2 and SCIAMACHY. *Journal of Geophysical Research: Atmospheres*, *122*(7), 4084-4111. https://doi.org/10.1002/2016JD025940

von Clarmann, T., Höpfner, M., Kellmann, S., Linden, A., Chauhan, S., Funke, B., et al. (2009). Retrieval of temperature, H_2O, O_3, HNO_3, CH_4, N_2O, $ClONO_2$ and ClO from MIPAS reduced resolution nominal mode limb emission measurements. *Atmos. Meas. Tech.*, *2*(1), 159-175. https://doi.org/10.5194/amt-2-159-2009

Walters, D., Baran, A. J., Boutle, I., Brooks, M., Earnshaw, P., Edwards, J., et al. (2019). The Met Office Unified Model Global Atmosphere 7.0/7.1 and JULES Global Land 7.0 configurations. *Geosci. Model Dev.*, *12*(5), 1909-1963. https://doi.org/10.5194/gmd-12-1909-2019

Whitlock, C. H., Bartlett, D. S., & Gurganus, E. A. (1982). Sea foam reflectance and influence on optimum wavelength for remote sensing of ocean aerosols. *Geophysical Research Letters*, *9*(6), 719-722. https://doi.org/https://doi.org/10.1029/GL009i006p00719

Xiong, X., Houweling, S., Wei, J., Maddy, E., Sun, F., & Barnet, C. (2009). Methane plume over south Asia during the monsoon season: satellite observation and model simulation. *Atmos. Chem. Phys.*, *9*(3), 783-794. https://doi.org/10.5194/acp-9-783-2009

Geophysical Research Letters

Supporting Information for

Methane's Solar Radiative Forcing

R. E. Byrom[1*] and K. P. Shine[1]

[1]Department of Meteorology, University of Reading, UK

[*]Current affiliation: CICERO Center for International Climate Research, Oslo, Norway

Contents of this file

Text S1.

SOCRATES-RF models the tropopause pressure (p_{trop}) based on the following parametric equation of Checa-Garcia et al., (2018), which describes a symmetrical tropopause between both hemispheres as:

$$p_{trop} = \delta \tanh[\beta^{-1}(|\phi| - \alpha)] + \gamma \quad \text{(S1)}$$

where ϕ is latitude, γ is the average of p_{trop} at 90° and 0°, δ defines the decrease in pressure between 90° and 0°, α defines the latitude at the centre of the transition from the 90° and 0° tropopause level (i.e. where $\tanh[\beta^{-1}(|\phi| - \alpha)] = 0$) and β defines the characteristic latitudinal width of the transition between the 90° and 0° tropopause. These parameters describe a tropopause without any seasonal dependence following the estimation of a climatological tropopause by Hansen et al., (2005). All SOCRATES-RF calculations use the combination of parameter values given in Table S1 to define p_{trop}. This yields an equatorial (0°) tropopause at 100 hPa and a polar (90°) tropopause at 230 hPa, resulting in a γ of 165 hPa (i.e. the average of 100 hPa and 230 hPa) and a δ of 65 hPa (which is defined as the difference between the tropopause at 90° and 0° divided by two i.e. δ = (230 hPa – 100 hPa)/2). At the latitude specified by α (i.e. 35°), p_{trop} equals γ; at latitudes either side of α, the tropopause varies according to Equation S1. Figure S1 shows the variation in p_{trop} with latitude as based on the parameters defined in Table S1.

$\boldsymbol{\delta}$	$\boldsymbol{\beta}$	$\boldsymbol{\gamma}$	$\boldsymbol{\alpha}$
65 hPa	10	165 hPa	35°

Table S1: Climatological tropopause parameters used to determine tropopause pressure in all SOCRATES-RF calculations. See Checa-Garcia et al., (2018).

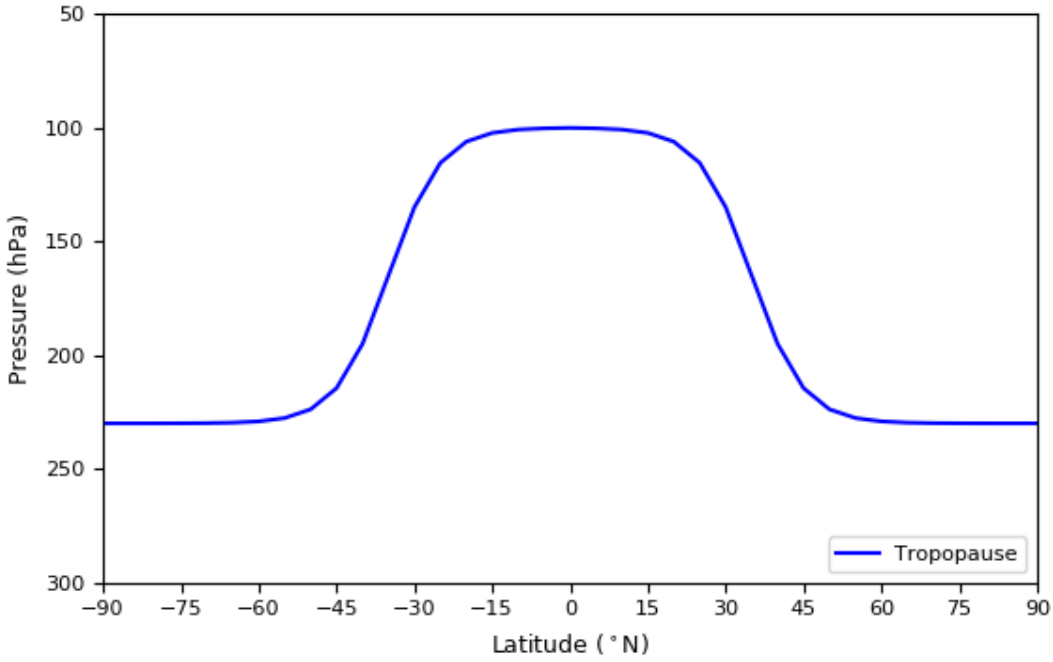

Figure S1: Variation in tropopause pressure with latitude as defined by Equation S1 and the parameters specified in Table S1. All SOCRATES-RF tropopause RFs are calculated using this definition of tropopause height.

Text S2

CH_4 mole fractions are derived from Michelson Interferometer for Passive Atmospheric Sounding (MIPAS) CH_4 climatology (Hegglin et al., 2021) created by the SPARC Data Initiative (SPARC, 2017). This dataset is comprised of monthly zonal-mean CH_4 mole fractions on a common latitude-pressure grid covering the upper troposphere to lower mesosphere (from 300 hPa to 0.1 hPa) with a latitudinal resolution of 5° from 87.5° north to 87.5° south (Figure S2). This climatology consists exclusively of measurements taken during the second MIPAS observation period (henceforth MIPAS-2) where the instrument operated with a reduced spectral resolution (but a higher vertical resolution) compared to its earlier 2002 – 2004 measurement mode (Plieninger et al., 2016). Hegglin et al., (2021) report that MIPAS-2 captures the extent and timing of high-latitude minima in CH_4 during the summer months (caused by photochemical reactions) and the semi-annual oscillation in CH_4 maxima in the tropical upper-stratosphere (caused by the upwelling of less depleted CH_4 air by the equatorial semi-annual oscillation; e.g. Choi and Holton, 1991).

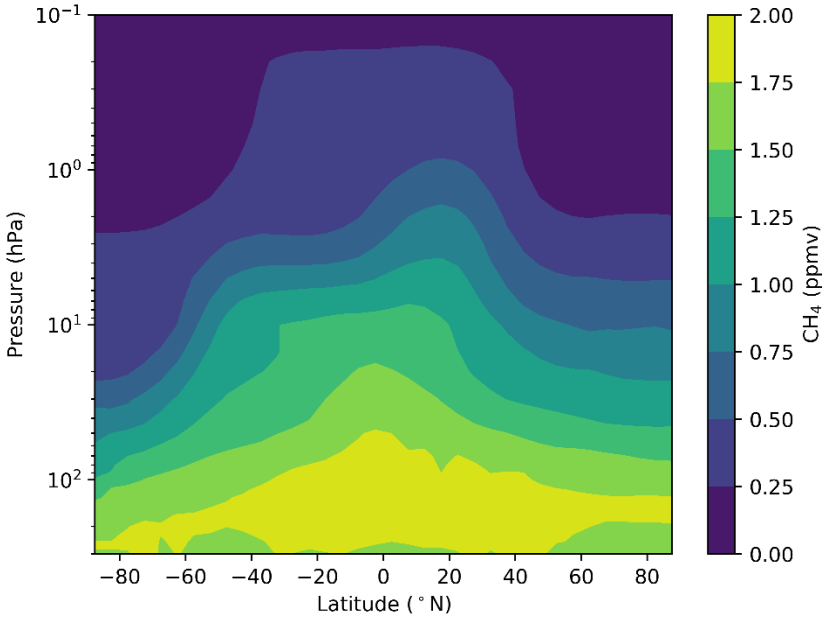

Figure S2: Zonal-mean, monthly-mean CH_4 mole fractions (in ppm) for July averaged over 2005 – 2012 showing maximum values high in the tropical upper troposphere.

Exploration of the MIPAS CH_4 climatology reveals that mole fractions in regions of the tropical upper troposphere are higher than those at higher pressure levels close to 300 hPa (where the highest mole fractions are typically expected to be found). Figure S2 displays this feature in zonal-mean, monthly-mean CH_4 for July. As shown, CH_4 maxima with values greater than 1.75 ppm (yellow filled contour) are evident across the equatorial region up to around 50 hPa. SPARC (2017) note that MIPAS-2 measurements exhibit a maximum in CH_4 in upper troposphere lower stratosphere (UTLS) region that is not present in other vertically-resolved SPARC satellite climatologies, such as the Atmospheric Chemistry Experiment-Fourier Transform Spectrometer (ACE-FTS) and the Halogen Occultation Experiment (HALOE) datasets.

This high bias is a known feature reported by several studies (e.g. von Clarmann et al., 2009; Laeng et al., 2015; Errera et al., 2016) and may be linked to instrument bias or the resulting impact of deep convection associated with the Asian monsoon region, which uplifts and traps high CH_4 mole fractions in the upper troposphere (Ricaud et al., 2014). Retrievals from the Atmospheric Infrared Sounder (AIRS) across 2003 – 2007 confirm the presence of strong CH_4 enhancement during the monsoon season in the middle to upper troposphere during July, August and September over South Asia (Xiong et al., 2009). The noted maxima in MIPAS-2 data may therefore occur as a result of such dynamical processes, which is missing from both ACE-FTS and HALOE due to sparser sampling of the

tropics by their solar occultation retrieval technique. However, it is unknown if such an enhancement in CH_4 would have been present in the pre-industrial era. Given that MIPAS-2 data are used to create monthly-mean pre-industrial fields of CH_4 in double-call RF calculations, this feature has been removed as follows:

1. At each latitude, pre-industrial CH_4 profiles are constructed using the fall-off rate of MIPAS CH_4 mole fraction, with a value of 750 ppb at 300 hPa.

2. All data points higher than 750 ppb at pressures lower than 300 hPa are masked and set to a value of 750 ppb.

This ensures that CH_4 mole fractions do not exceed 750 ppb at altitudes higher than 300 hPa. Figure S3 shows the resulting zonal-mean, monthly-mean pre-industrial CH_4 mole fractions for July.

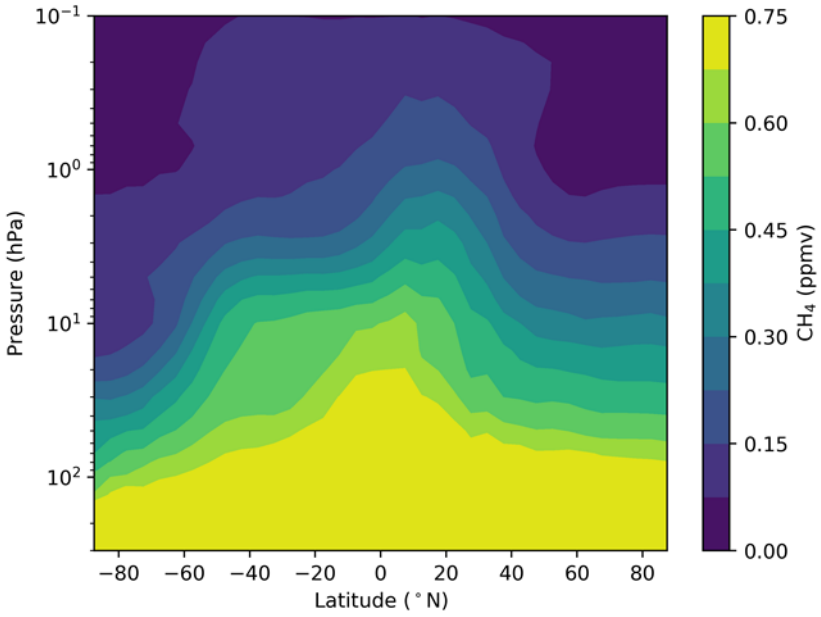

Figure S3: Pre-industrial zonal-mean, monthly-mean CH_4 for July (averaged over 2005 – 2012). Constructed using the fall-off rate of MIPAS CH_4 mole fraction with a value of 0.75 ppm at 300 hPa. The localised maxima in the tropical upper-troposphere in MIPAS CH_4 (see Text S2) has been removed by masking all data points higher than 0.75 ppm at pressures lower than 300 hPa to a value of 0.75 ppm.

Following this, MIPAS CH_4 fields are incorporated into SOCRATES-RF simulations as follows:

1. At each latitude, pre-industrial CH_4 profiles are constructed using the fall-off rate of MIPAS CH_4 mole fractions, with a value of 750 ppb at 300 hPa. This assumes that processes determining the fall off rate (and its monthly and latitudinal variation) are unchanged relative to the present day.

2. Data are regridded to a 5° x 5° spatial resolution to match the latitudinal and longitudinal coordinates of monthly-mean ERA-interim (Dee et al., 2011) climatological fields.

3. Data are interpolated to monthly-mean ERA-interim pressure levels, resulting in constant CH_4 throughout the troposphere and vertically-varying CH_4 in the stratosphere.

Text S3

Version 2.6 of the SCIAMACHY LER database (Tilstra et al., 2017) provides a climatology of Earth's surface reflectivity across 34 one-nm wavelength bands between 0.328-2.314 μm for each month of the year averaged between 2002-2012 at a 0.5° x 0.5° spatial resolution (https://www.temis.nl/surface/albedo/scia_ler.php last accessed 27/10/21). In this paper 33 bands between 0.355-2.314 μm are used to provide lower boundary conditions in SOCRATES-RF calculations. Data at 0.328 μm are excluded because surface reflectivity at this wavelength contributes a small amount to TOA reflectance (see Tilstra et al., 2017). Tilstra et al., (2017) examine the spatial, temporal and spectral behaviour of SCIAMACHY α_s and report good agreement with databases derived from the Total Ozone Mapping Spectrometer (TOMS), Global Ozone Monitoring Experiment (GOME-1 and GOME-2) and the Ozone Monitoring Instrument (OMI). Crucially, SCIAMACHY data cover a wider wavelength range than alternative datasets and thereby provide a measure of surface reflectivity at wavelengths important for CH_4 SW absorption (i.e., at 1.7 μm and 2.3 μm).

In this paper all SCIAMACHY α_s data are obtained following the MODE-LER approach - a new statistical method presented by Tilstra et al., (2017) which better determines the retrieval of surface LER from cloud-free satellite scenes. Initial handling of the database reveals α_s values above one occur multiple times in each month in several different wavebands (mostly in the VIS), predominantly across the high-latitude and polar regions. It is not known why this occurs and inspection of the accompanying metadata did not

provide an explanation. To handle this, all α_s values above one were replaced with a value of 0.95 (Huang et al., 2018).

Figure S4 presents a schematic of the method used to interpolate and extrapolate SCIAMACHY α_s to the upper wavelength limit of each band in sp_sw_260_jm2.

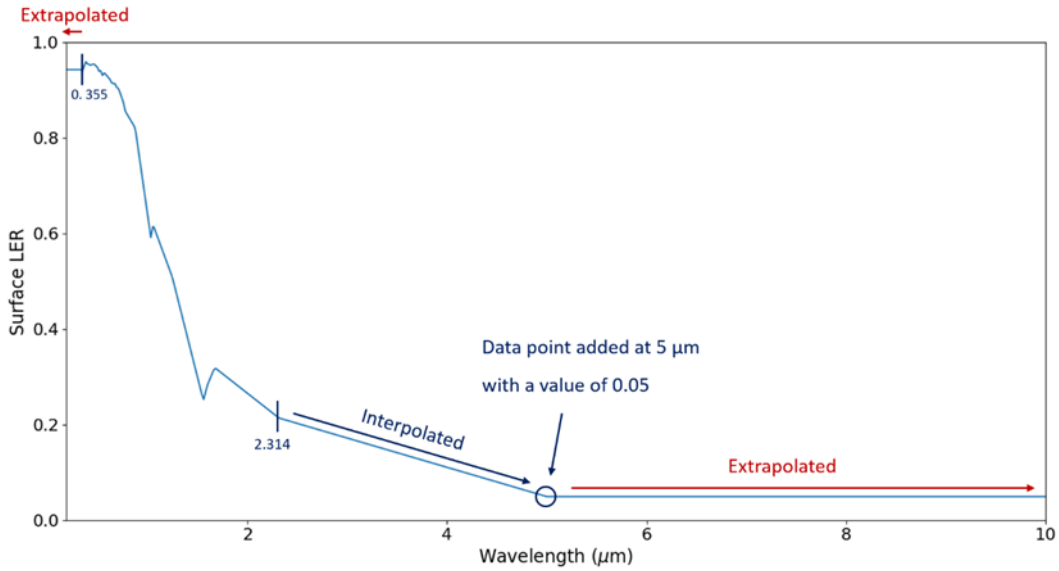

Figure S4: Schematic of the method used to assimilate SCIAMACHY spectral α_s data (Tilstra et al., 2017) into SOCRATES-RF's SW spectral file, sp_sw_260_jm2. This example demonstrates the process at a snow-covered grid-point located at 70°N, 155°W, Alaska for the month of May.

Data are linearly interpolated to the upper wavelength limit of each sp_sw_260_jm2 band between 0.355 and 2.314 μm. An additional α_s datapoint is constructed at 5 μm with a value of 0.05 to extend spectral reflectance to wavelengths greater than 2.314 μm. Huang et al., (2018) show that surface emissivity (ε) at wavelengths above 5 μm are around 0.95 for a range of land surface types such as water, ice, snow and desert. A value of 0.05 is therefore adopted assuming:

$$\alpha = 1 - \varepsilon \quad \text{(S2)}$$

To extend spectral reflectance to the upper and lower bands of sp_sw_260_jm2, data are linearly extrapolated from 5 to 10 μm and from 0.355 to 0.17 μm. Given the lack of monthly, global albedo datasets at wavelengths greater than 2.314 μm and less than 0.328 μm, this approach constructs a best estimate of spectral surface reflectance across

the 0.17 to 10 μm range. It is acknowledged that this method could be significantly improved if such global datasets became available.

Further handling of the database revealed low spectral surface albedo values (around 0.001 to 0.008) across the NIR region over the global oceans. As stated in the main text, these values are judged to inadequately represent the spectral reflectance of sea-surfaces which depend on a variety of complex factors, such as wind-induced variations in surface roughness, salinity, the effect of ocean whitecaps and marine biogeochemistry (e.g. Briegleb and Ramanathan, 1982; Roesch et al., 2002; Séférian et al., 2018). Subsequently, all sea-surface datapoints are masked and replaced with spectrally-varying α_s calculated using a SOCRATES internal subroutine. This subroutine accounts for the spectral variation of sea-α_s due to Fresnel reflection, modified to account for the impact of wind-induced variations in sea-surface roughness following Cox and Munk (1954), assuming nominal values for 10 metre wind speed of 7 m s^{-1}. Refractive indices of water are taken from Jerlov (1976) and Hale and Querry (1973), modified for nominal values of sea surface salinity of 35 g kg^{-1}. The effect of ocean whitecaps are also included from Whitlock et al., (1982); however this makes a small contribution to spectral reflectance given that whitecaps typically account for less than 2% of the sea-surface. Since sea-α_s is dependent on solar zenith angle, α_s is calculated assuming a daylight-average solar zenith angle at each grid-point and month. This scheme is of similar complexity to the representation of sea-surface albedo in Collins et al., (2018) and is more sophisticated than models such as the European Centre for Medium-range Weather Forecasts Integrated Forecasting System (ECMWF-IFS), where no spectral variation is assumed (IFS Documentation CY47R1, 2020). Much more sophisticated sea-surface parameterisations are available, for example Séférian et al., (2018). However, these require the specification of many more parameters, such as biophysical processes that govern the interaction of solar radiation with marine chlorophyll, and spatially and temporally varying surface wind speeds.

Text S4

The following description, taken from Collins et al., (2004)[1], outlines how CAM 3.0 CH_4 scale-heights are derived:

Globally, tropospheric CH_4 is assumed to be well mixed and are prescribed in units of mass mixing ratio (MMR) as follows:

$$\mu^0_{CH_4} = 0.554 w_{CH_4} \quad \text{(S3)}$$

where w_{CH_4} denotes the volume mixing ratio of CH_4. Above the tropopause CH_4 MMRs are specified as zonally-averaged quantities that vary with latitude to imitate the effect of stratospheric circulation and chemistry on CH_4. The pressure level of the tropopause (in hPa) is defined by:

$$p_{trop} = 250.0 - 150.0\, cos^2\phi \quad \text{(S4)}$$

where ϕ denotes latitude.

Following this, for $p \leq p_{trop}$, stratospheric CH_4 MMRs are defined as:

$$\mu_{CH_4} = \mu^0_{CH_4} \left(\frac{p}{p_{trop}}\right)^{X_{CH_4}} \quad \text{(S5)}$$

where X_{CH_4} denotes the mixing ratio scale heights. For $|\phi| \leq 45°$,

[1] Two errors were found in this description of CH_4 mixing ratio scale-heights. Both related to Equation S7, reported originally by Collins et al., (2004) as: $X_{CH_4} = 0.2353 + 0.22549(\phi)$. See Equation S7 for corrections. We thank William D. Collins for providing clarification.

$$X_{CH_4} = 0.2353 \tag{S6}$$

and for $|\phi| > 45°$,

$$X_{CH_4} = 0.2353 + 0.022549(\phi - 45) \tag{S7}$$

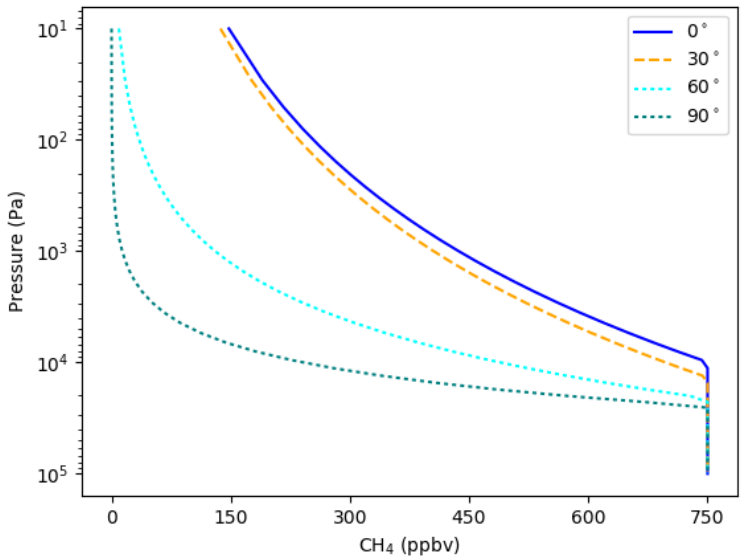

Figure S5: Zonal-mean vertically-varying CH_4 profiles at 0°, 30°, 60° and 90° latitude. CH_4 is well-mixed throughout the troposphere at 750 ppb and decreases exponentially above the tropopause as per the CAM 3.0 latitude-dependent mixing ratio scale height given by Equation S5. Note that the profile at 90° does not drop to zero completely, however it reaches a minimum of 0.04 ppb at 10 Pa. Also note that this equation does not model hemispherical and seasonal differences in mixing ratio scale heights. The profiles at the four latitudes shown here are therefore representative of both the northern and southern hemispheres for each month of the year.

Figure S6

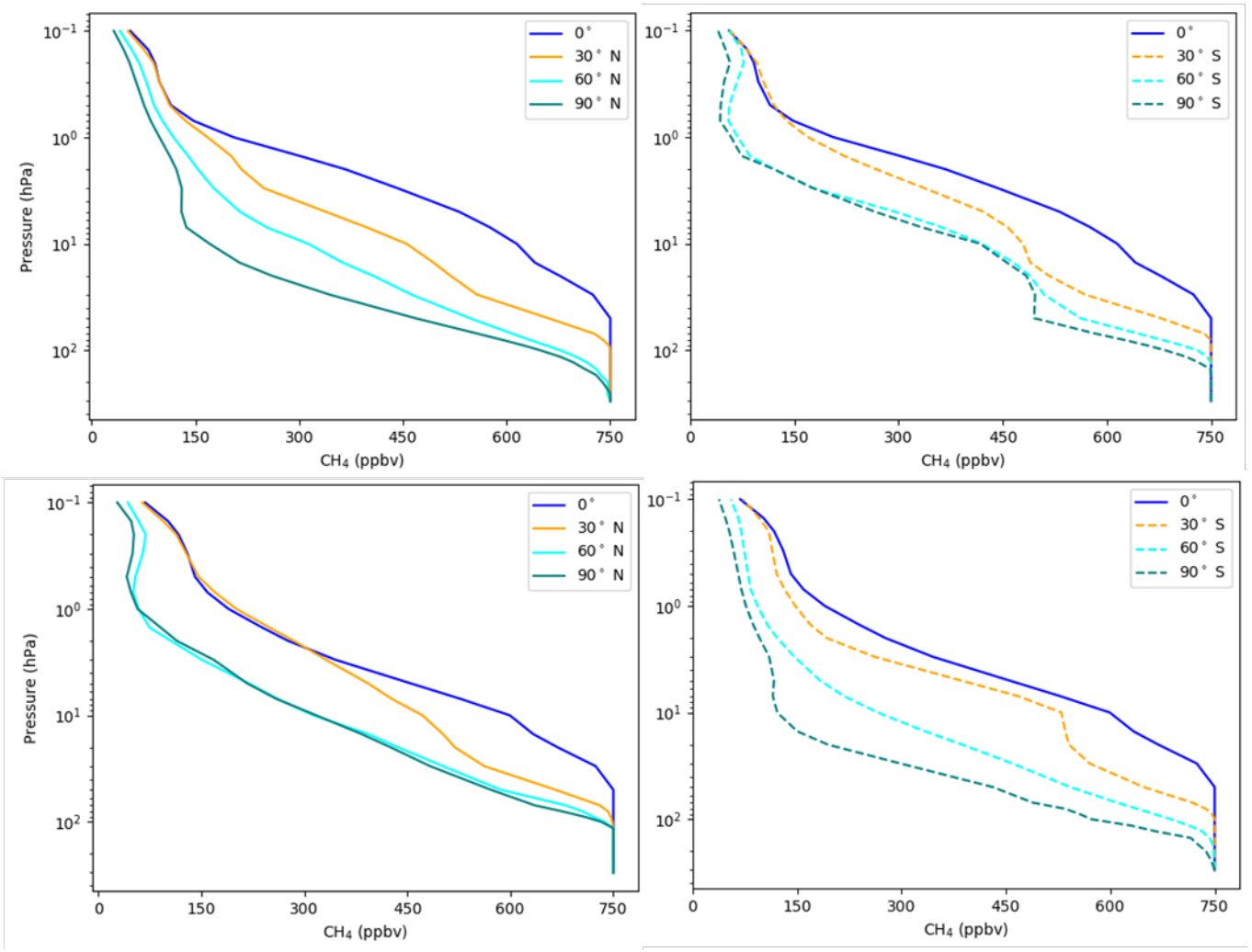

Figure S6: Pre-industrial (750 ppb) zonal seasonal-mean CH_4 profiles for DJF (upper panel) and JJA (lower panel) at 0°, 30°, 60° and 90° north (left-hand side) and south (right-hand side) constructed using MIPAS zonal-mean CH_4 fall off rate as described in Text S2.

Figure S7

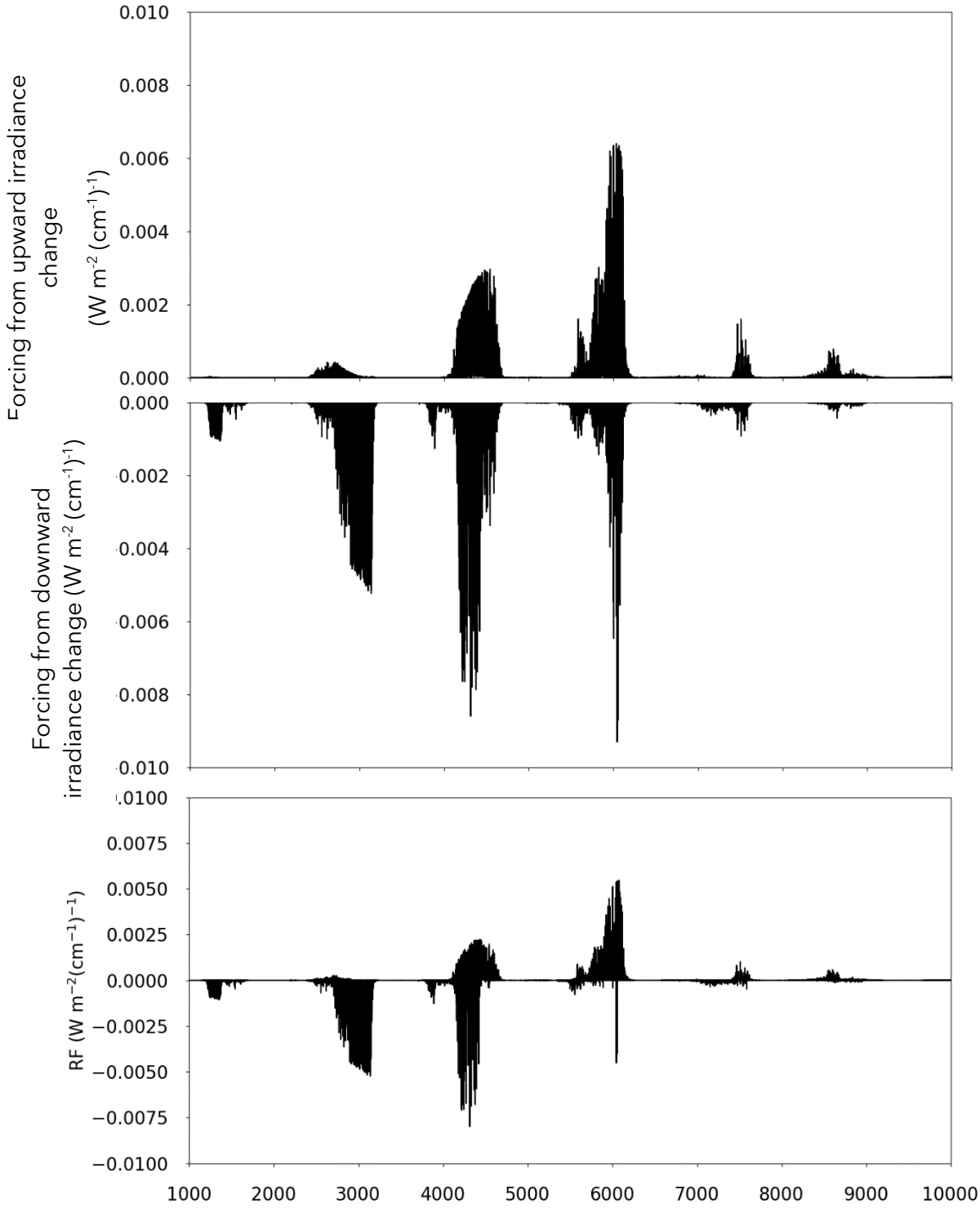

Figure S7: Spectral variation of upwelling (top) and downwelling (middle) CH_4 SW IRF components at the tropopause and the corresponding net tropopause IRF (lower) following a perturbation in CH_4 from 850 ppb to 1700 ppb using atmospheric data from Case 6 of Phase I of the Continual Intercomparison of Radiation Codes (CIRC) experiments (Oreopoulos et al., 2012).

Figure S8

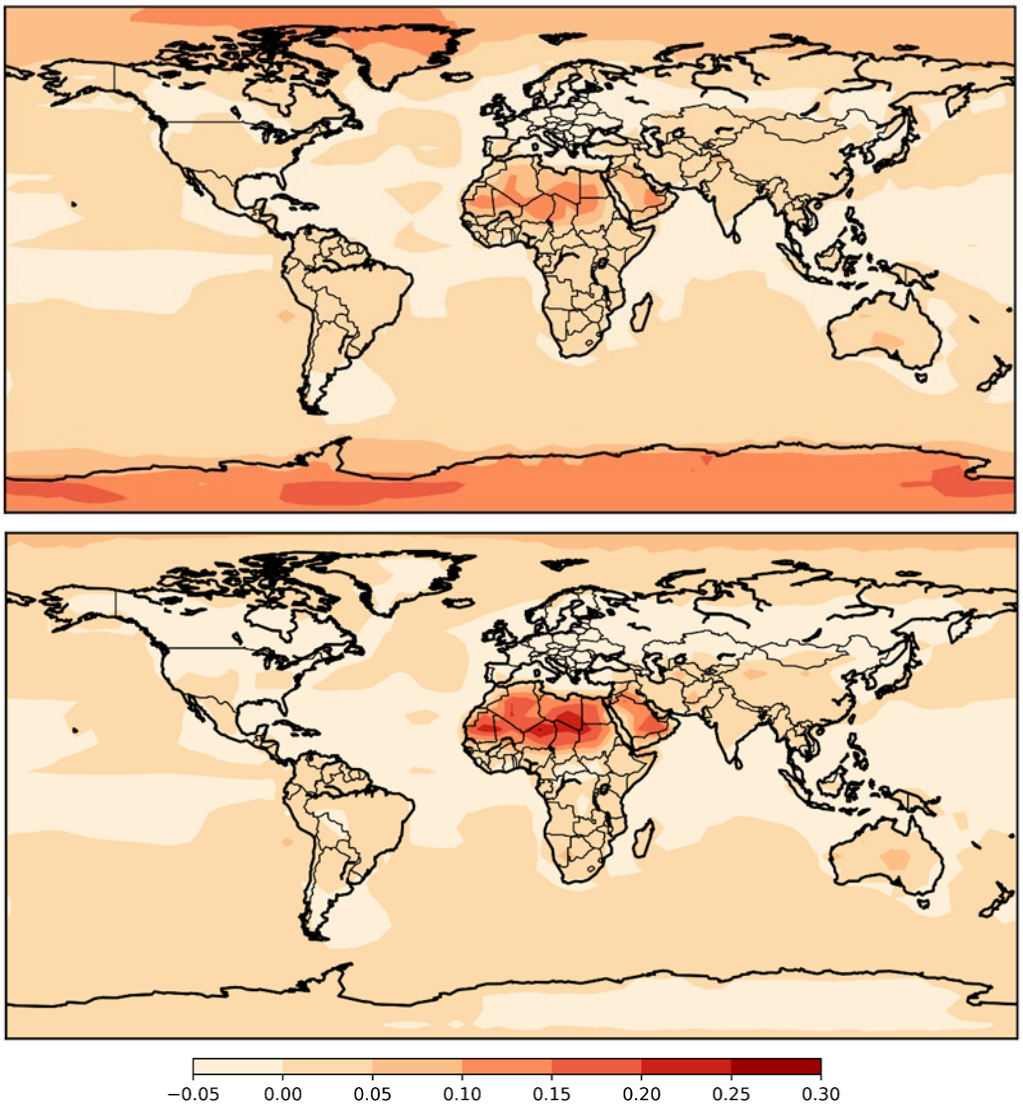

Figure S8: The impact of using spectrally-constant and spectrally-varying surface albedos on CH_4 SW IRF. Upper panel: Quasi-annual all-sky SW tropopause IRF (W m^{-2}) derived using CAM 3.0 CH_4 mole fraction scale-heights and monthly-mean fields of spectrally-constant ERA-interim α_s. Lower panel: Quasi-annual all-sky SW tropopause IRF (W m^{-2}) derived using CAM 3.0 CH_4 mole fraction scale-heights and SCIAMACHY-SSA α_s. Both are derived following a perturbation in CH_4 from 750 to 1800 ppb. Note that these estimates represent quasi-annual calculations from the four mid-season months (January, April, July and October). Analysis demonstrates that the average of these months (referred to here as the quasi-annual mean) serves as a good representation of the full 12-month annual mean for the purpose of sensitivity tests. In the main text, all reported forcings are full 12-month annual means except where indicated.

Text S5

Multi-model intercomparison studies provide a useful basis from which to assess uncertainty in radiative transfer schemes used in forcing calculations (e.g. Collins et al. 2006; *Pincus et al.*, 2015). However, there is lack of research comparing broad-band radiative transfer codes against benchmark calculations specifically for CH_4 SW RF, largely because many ESM radiation codes have historically omitted explicit treatment of CH_4 SW absorption (e.g. Collins et al. 2006). We repeated our calculations using the current 6-band SOCRATES SW spectral file configuration (sp_sw_ga7) used in the Met Office Unified Model; it significantly underestimates CH_4 SW tropopause and surface IRF by around 45% compared to the 260-band configuration. Hogan and Matricardi (2020) also report an underestimation of CH_4 SW IRF by 25 – 45% by the Rapid Radiative Transfer Model for General Circulation Models (RRTMG) (Mlawer et al., 1997) compared to benchmark calculations for perturbations across 350 to 3500 ppb. As stated in Section 2, the 260-band SOCRATES SW spectral file has been validated here against the RFM. Under a range of atmospheric conditions and CH_4 SW IRF scenarios, sp_sw_260_jm2 exhibits a mean error of 8%. Uncertainty associated with the 9-band SOCRATES LW spectral file is assessed to be 6% considering prior research (e.g. Collins et al., 2006) and validation by Walters et al., (2019).

Hodnebrog et al., (2013; 2020) discuss error in RF calculations based on a multitude of previous studies to assess uncertainty related specifically to halocarbon RF; their discussion can be used more generally to assess error in other well-mixed GHG forcings (e.g. Etminan et al., 2016) and is used here to estimate the following uncertainties: the calculation of FDH (4%), atmospheric temperature (3%) and clouds (5%) and spatial and temporal averaging (1%). Hodnebrog et al., (2013) assess uncertainty related to tropopause height to be around 5%. Here, this uncertainty is assessed to be 10% for CH_4 SW tropopause IRF and 5% for CH_4 LW SARF. A higher value is attributed to SW calculations owing to the particular sensitivity of CH_4 SW tropopause IRF to the magnitude of upward and downward forcing components.

An additional important error source relates to the specification of α_s. The method used to interpolate and extrapolate SCIAMACHY data is idealised, owing to a lack of global datasets that extend across 0.17-10 μm. An uncertainty of 20% is tentatively attributed to the use of SCIAMACHY-SSA α_s. Furthermore, idealised tests demonstrate significant sensitivity of CH_4 SW IRF to the representation of H_2O self-continuum absorption. Using the analysis of laboratory data in Anisman et al., (2022), a modified sp_sw_260_jm2 spectral file with a reduced self-continuum strength in the 2.1 μm window causes a 5% difference in January clear-sky CH_4 tropopause SW IRF (-0.039 W m^{-2}) for a 750-1800 ppb perturbation compared to the unmodified spectral file (-0.041 W m^{-2}). Similarly, the specification of H_2O fields is a potential error source given the dependence of CH_4 SW IRF on H_2O spectral overlap (Etminan et al., 2016). Collins et al., (2018) find that SW forcings differ by around 32% under clear-sky conditions and 4% under all-sky conditions, depending on which ESM background climatology is used (Table 2, Collins et al., 2018). Here, uncertainty related to H_2O fields is assessed to contribute 2% to total uncertainty in all-sky CH_4 SW tropopause IRF and LW SARF.

Finally, considering the sensitivity of CH_4 SW IRF to vertical profile specification, an uncertainty of 5% is attributed to the use of MIPAS CH_4 climatology based on the standard deviation of multi-instrument spread in CH_4 measurements (Hegglin et al., 2021). A lower uncertainty of 2% is attributed to the use of MIPAS CH_4 climatology in CH_4 LW SARF, as this calculation is not significantly dependent on CH_4 profile specification (e.g., Freckleton et al., 1998).

As summarised in the main text, we calculate uncertainty using the root-sum-square method. A total uncertainty of ±12% is attributed to CH_4 LW SARF and a total uncertainty of ±25% is tentatively attributed to CH_4 SW tropopause IRF. Overall, given that the CH_4 SW effect is about 6% of the net CH_4 SARF, this yields a total uncertainty of around ±13% in net CH_4 SARF.

Source of Uncertainty	Estimated Contribution to SW Uncertainty	Estimated Contribution to LW Uncertainty
Spectroscopic parameters	1%	1%
SW radiation code	8%	-
LW radiation code	-	6%
H_2O continuum	5%	Not assessed
FDH calculation	-	4%
Tropopause level	10%	5%
Atmospheric temperature	-	3%
Clouds	5%	5%
H_2O field	2%	4%
Spatial and temporal averaging	1%	1%
MIPAS CH_4 mole fractions	5%	2%
SCIAMACHY-SSA α_s	20%	-
Total uncertainty	**25%**	**12%**

Table S2: Sources of uncertainty and their estimated contribution to total uncertainty in estimates of CH_4 SW tropopause IRF and CH_4 LW SARF calculated using MIPAS CH_4 mole fractions and SCIAMACHY-SSA α_s. The total uncertainty is also shown and is calculated using the root-sum-square method. See Text S5 for references used as basis for uncertainty estimates.